POLITECNICO DI MILANO
Degree of Master of Science in Aeronautic Engineering
School of Industrial and Information Engineering

Numerical Simulation of Underexpanded Jets in the Non-ideal Flow Regime

Supervisor: Professor Alberto Matteo Attilio Guardone
Co-supervisor: Dr Camilla Cecilia Conti

Author: PENG YAN
Matriculation number: 936041

Academic year 2021-2022

Acknowledgment

Here, I want to show my thanks to everyone who gives me a hand when I worked on final thesis. Firstly, I want to say thanks to professor Alberto Matteo Attilio Guardone. It is him who leads me to underexpanded jet flow, which is an interesting field. In addition, I am grateful to Dr Camilla Cecilia Conti. She helps me a lot, including how to set up numerical simulation in SU2, instruct and correct my final thesis with patience. Without her, I can not finish the thesis with high quality on time. Also, I say thanks to my families, my friends, who support me during hard time, especially under COVID-19 virus pandemic.

Contents

List of Figures

List of Tables

Abstract

Abstract: Numerical simulations of ideal and non-ideal jet flows are carried out based on open source software SU2. Two categories of simulations with different nozzle reservoir-to-ambient pressure ratio are investigated. Each category includes four types of test cases: ideal inviscid, non-ideal inviscid, ideal viscous, non-ideal viscous flow. In each type of flow, cases with different pressure level are carried out. Polytropic ideal gas model is used for ideal flow while van der Waals model is applied for non-ideal flow. Firstly, the simulation results of ideal inviscid flow are compared with previous work and it shows that results in this work are reliable. Further, by comparing different types of test cases, the effects of non-ideality, pressure ratio, pressure level, viscosity are investigated.

Sommario: Le simulazioni numeriche di getti ideali e non ideali sono utilizzando del software open source SU2. Vengono studiate due categorie di simulazioni con diverso rapporto tra serbatoio e pressione ambiente dell'ugello. Ogni categoria comprende quattro tipi di casi studio: ideale non viscoso, non ideale non viscoso, ideale viscoso, flusso viscoso non ideale. In ogni tipo di flusso vengono simulati casi con diverso livello di pressione. Il modello di gas ideale politropico viene utilizzato per il flusso ideale mentre il modello di van der Waals viene applicato per il flusso non ideale. In primo luogo, i risultati della simulazione del flusso ideale non viscoso vengono confrontati con lavori precedenti precedente e mostra che i risultati di questo lavoro sono ragionevoli. Inoltre, confrontando diversi tipi di casi di test, si trovano gli effetti di non idealità, rapporto di pressione, livello di pressione, viscosità.

Chapter 1

Introduction

1.1 Non-Ideal Compressible Fluid Dynamics

For dense gases operating condition near the liquid-vapor saturation curve and critical point, their thermodynamic behaviors largely differ from that of polytropic ideal gas (PIG). The flow dynamics in this special regime is the research core of Non-Ideal Compressible Fluid Dynamics (NICFD), which is a novel branch of fluid dynamics.

PIG is the simplest and most used gas model in gas dynamics field since it can provide a supplement equation to help close the governing equations. In most cases of dilute gases, PIG model is accurate enough for theoretical calculations or numerical simulations. However, a big discrepancy from PIG thermodynamic behaviors can be found in the dense gas regime when approaching the liquid-vapor saturation curve and critical points. This is because the intermolecular forces can not be neglected any more, which was firstly noticed by Van der Waals[5]. To include this factor, more complicated gas models are proposed, like Van der Waals model, Berthelot model[6], Peng-Robinson model[7] and so on. These gas models are different from PIG model and hence they are called non-ideal gas model or real gas model.

In terms of thermodynamics, the boundary between ideal gas and non-ideal gas can be delimited by a dimensionless parameter: *compressibility factor* $Z = \frac{Pv}{RT}$, where P, ν, R, T are pressure, specific volume, specific gas constant and temperature. For PIG, $Z = 1$ and for non-ideal gas, $Z \neq 1$. Meanwhile, from standpoint of gasdynamics, another non-dimension parameter is used: *the fundamental derivative of gasdynamics*, Γ[2], which is defined as following:

$$\Gamma = \frac{v^3}{2c^2}(\frac{\partial^2 P}{\partial v^2})_s = 1 + \frac{c}{v}(\frac{\partial c}{\partial P})_s \tag{1.1}$$

where c the speed of sound and s the specific entropy. Γ is important in gasdynamics because it can be used to measure how speed of sound changes along an isentropic process.. For PIG, the expression of Γ is very simple, i.e., $\Gamma = (\gamma + 1)/2$, where the ratio of specific heats $\gamma > 1$ and as a result, $\Gamma > 1$, too. Flow field of $0 < \Gamma < 1$ is referred as *non-ideal regime* while that of $\Gamma < 0$ is called *non-classical regime.* The classification is depicted in figure 1.1. In non-

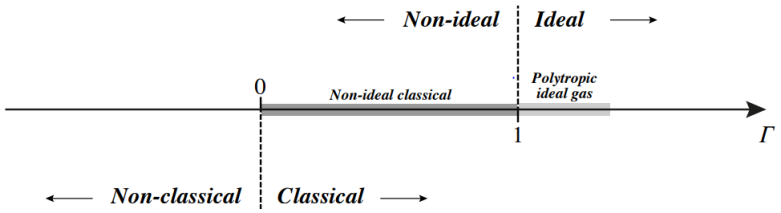

Figure 1.1: Classification of flow regimes[1]

ideal flow regime, some unusual phenomenons which are opposite from PIG can be observed. A typical case is that the speed of sound increase with expansion with $\Gamma < 1$ and hence the Mach number may not decreases across the oblique shock[8]. Thompson derived the analytic solutions for various Γ and behaviors of fluid properties along the isentrope is shown in figure 1.2.

Γ	Behavior
$\Gamma > 1$	Soundspeed increases with P; behavior of usual substances.
$\Gamma = 1$	Constant soundspeed; P a linear function of $\rho = 1/\mathcal{V}$.
$0 < \Gamma < 1$	Soundspeed decreases with P.
$\Gamma = 0$	P a linear function of $\mathcal{V}$.
$\Gamma < 0$	Negative curvature of isentrope; behavior of unusual substances.

Figure 1.2: Behaviors of fluid properties along the isentrope[2]

Non-ideal flow is very common and can be found in many practical applications. A supersonic nozzle flow of N_2O near supercritical condition is applied in engine of aircrafts. [9]. Supercritical CO_2 is popular in pharmaceutical industry[10] and food processing[11] due to its $Z < 1$ near critical points. An important application area is Organic Rankine Cycle(ORC), in which the working fluids can have highly complex molecules, like MDM[12], and passes the non-ideal flow regime.

Considering the common occurrence of non-ideal flow, people have put lots of effort on researching this field. Theoretical part has been developed much recently[13], although still incomplete com-

pared with PIG. Experiments data related to non-ideal flow are less available since it is difficult to carry out experiment under environment with high pressure and temperature. Despite the difficulty, experiment work is being investigated, including Ludwieg-type shock tube FAST[14], the supersonic blow-down wind tunnel TROVA at Politecnico di Milano[15], the supersonic closed-circuit wind tunnel ORCHID at Delft University of Technology[16]. In addition, numerical softwares are also useful to obtain reliable solutions, e.g., FlowMesh[17], Openfoam[18], SU2[19].

1.2 Underexpanded jets of polytropic ideal gas

In compressible fluid dynamics area, a typical research prototype is the converging-diverging nozzle flow. For quasi-1D steady nozzle flow, the flow features only depend on the reservoir-to-ambient pressure ratio P_0/P_a, independent on the absolute pressure value. When the pressure ratio is sufficiently high, the flow in a convergent-divergent nozzle is subsonic-sonic-supersonic and the pressure at the nozzle exit P_e is higher than the ambient pressure P_a. Such kind of flow is called *underexpanded flow*. For underexpanded jet, there exist complex flow structures outside the nozzle, including shock, reflected shock, Mach disk, slip line, etc, which will be explained in details in section 2.1.2. The complex flow structures have been verified numerically[3] and experimentally[4]. Due to this reason, underexpanded jet is a good candidate for computational fluid dynamics(CFD), e.g., for the mesh adaptation assessment[17]. Underexpanded jets are of interest in particle nucleation[10], exhaust plumes of space shuttle propulsion system[20], ORC turbines with organic compound substances of highly complex molecule structures.

1.3 Underexpanded jets of non-ideal gas

NICFD plays a role in underexpanded jets and the flow field of non-ideal gas differs from that of ideal gas. For example, it was found that contrast with PIG, for polytropic Van der Waals gas, the flow features depend on not only the reservoir-to-ambient pressure ratio P_0/P_a, but also the reservoir conditions[3]. With const pressure ratio but higher P_0, the Mach disk radius decreases while its distance to the nozzle exit increases. The numerical solution of pressure distribution along the center axis agrees with the experiment result well until the Mach disk[4]. However, the total pressure after Mach

disk from experiment data increases rapidly while it changes a little from numerical solution. The author of the paper[4] thought that the possible reason was due to lack of viscosity in numerical simulation, which could transfer momentum from outside the slip line. Besides, non polytropic gas, which means the ratio of specific heats γ is not constant, ,was also investigated and the numerical result showed that flow variables distribution changed a lot[21]. Also, numerical analysis of hydrogen underexpanded jets using real gas model was carried and the results verified the real gas effect near the critical points[22]. Experiments of non-ideal underexpanded jets are carried out[23].

1.4 Research motivations and objectives

Despite that there are many research results on non-ideal underexpanded jets, some problem are still not completely understood. How the Mach disk is affected by the pressure-to-ambient pressure ratio, pressure level at the nozzle exit, viscosity and non-ideality are not known yet.

Hence, the objective of this work is to answer the above questions by carrying out numerical simulations based on open CFD software SU2, and compare with previous numerical and experimental results. Once these questions are solved, the conclusion can be applied directly and helpful for operation of ORC turbines, food-process industry and so on.

1.5 Summary of the thesis

The thesis is organized as follows.
Chapter 2 simply introduces the theory of isentropic nozzle flow and then describes the flow features of underexpanded jet outside the nozzle. The theoretical mechanism about how the Mach disk forms is explained qualitatively. In addition, basic background associated with numerical simulation is introduced, including the governing equations, thermodynamic model, numerical simulation setup, as well as geometry and boundary condition of computational domain.
Chapter 3 reports the main results of numerical simulations. All simulation are divided into two categories, depending on the reservoir-to-ambient pressure ratio is 8 or 10. In each category, four types of simulations are carried out,including ideal inviscid, non-ideal inviscid, ideal viscous and non-ideal viscous cases. For each type, exit-to-ambient pressure ratio is kept constant but higher pressure P_e

is applied to evaluate whether Mack disk is influenced by pressure level.

Chapter 4 summarizes the conclusions by comparing various results and further possible research directions.

Chapter 2

Theory and Numerical methods

2.1 Steady compressible dynamics

2.1.1 Isentropic flow in a nozzle

For isentropic flow of PIG, the value of pressure, temperature, density can be computed from Mach number according to the following formulations:

$$\frac{T^t}{T} = [1 + \frac{\gamma - 1}{2} M^2] \tag{2.1a}$$

$$\frac{P^t}{P} = [1 + \frac{\gamma - 1}{2} M^2]^{\frac{\gamma}{\gamma - 1}} \tag{2.1b}$$

$$\frac{\rho^t}{\rho} = [1 + \frac{\gamma - 1}{2} M^2]^{\frac{1}{\gamma - 1}} \tag{2.1c}$$

where symbols with superscript ^{t} indicates the total values; γ is the ratio of specific heats and M is the Mach number. Although this formulation is derived for invicid PIG, it can be also used for non-ideal and viscous flow for preliminary estimation.

2.1.2 Mach disk outside the nozzle

When the reservoir-to-ambient pressure ratio P_0/P_a is higher than the ratio related to adapted nozzle condition, the pressure at the nozzle exit P_e is higher than ambient pressure P_a and the flow in a nozzle is subsonic-sonic-supersonic without shock inside nozzle. This kind of flow is called *underexpanded jet flow.*

The basic flow features of underexpanded jet flow are sketched in figure 2.1. According to the exit-to-ambient pressure ratio, there

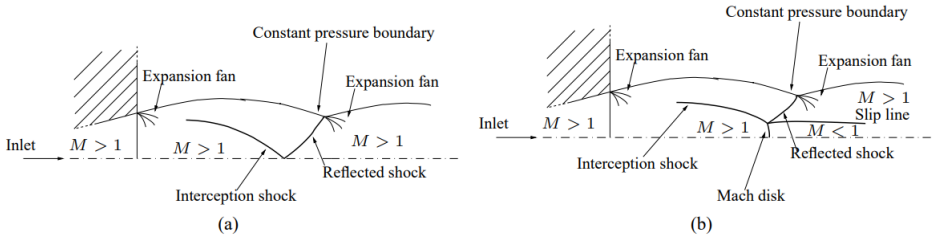

Figure 2.1: Flow field of underexpanded jet[3]:(a)regular (b)irregular

are two kinds of underexpanded jet. The first one is weakly or regular(case a) and the second one is strongly or irregular(case b). Generally, since exit pressure P_e is higher than ambient pressure P_a, Prandtl-Mayer expansion waves form at the exit section. These waves reflect from the constant pressure boundary and becomes compression waves, which subsequently coalesce to form interception shock. The interception shock reflects at the centerline and forms reflected shock. This process leads to a regular underexpanded jet.

However, if the exit-to-ambient pressure ratio is higher than that of a regular underexpanded jet, then an irregular underexpanded jet forms. Along the centerline, the pressure decreases due to the expansion waves, and in some region, the pressure is lower than ambient pressure P_a. Then an adverse pressure gradient is required to make the pressure up to P_a. If the adverse pressure gradient is large over a short distance, a Mach disk is generated, as shown in figure 2.1 case b. This phenomenon can also be explained in terms of interaction between outer flow and centerline flow. As pointed out by Crocco[24], it is not sufficient to generate a large adverse pressure gradient considering interaction between supersonic centerline flow and supersonic outer flow. Hence, the centerline flow must be subsonic, which can be achieved only by crossing a Mach disk. More details of theoretical mechanism can be found in [25].

2.2 Numerical method and thermodynamic model

2.2.1 Governing equations

The governing equations for steady, compressible, inviscid, symmetric flow are steady compressible Euler equations in cylindrical coordinates. Reynolds-Averaged-Navier-Stokes (RANS) equations are applied for viscous flow, in which turbulence model is considered.

2.2.2 Thermodynamic model

To obtain the specific expression of pressure function in governing equations, two additional equations of state (EOS) are needed: pressure $P = P(T, v)$, internal energy $e = e(T, v)$, where T is the temperature and v is the specific volume. For PIG, these two EOS are simple:

$$P = \rho RT, e = \frac{RT}{\gamma - 1} \tag{2.2}$$

where $R = \mathcal{R}/\mathcal{M}$ is the specific gas constant, with $\mathcal{R} = 8.314 J/(molK)$ the universal gas constant and $\mathcal{M}$ the molecular weight of gas. However, for non-ideal gases, the intermolecular forces play a role and hence a more accurate EOS accounting for them is required. The simplest real gas model is polytropic van der Waals model, which is accurate enough to capture the non-ideal gas effect. The equations of states for van der Waals gas are:

$$P(T, v) = \frac{RT}{v - b} - \frac{a}{v^2}, e(T, v) = c_v T - \frac{a}{v} \tag{2.3}$$

where a is a parameter which is gas-dependent on long range attractive intermolecular forces, while b is associated with short range repulsive intermolecular forces. c_v is the specific heat at constant volume. The values of a and b can be obtained by considering the equilibrium conditions at critical points:

$$(\frac{\partial P}{\partial v})_T = 0 \tag{2.4a}$$

$$(\frac{\partial^2 P}{\partial v^2})_T = 0 \tag{2.4b}$$

which leads to the expression of a and b:

$$a = \frac{27R^2T_c^2}{64P_c}, b = \frac{RT_c}{8P_c} \tag{2.5}$$

where symbols with subscript c indicates values at critical condition.

2.2.3 Numerical simulation setup

Once the governing equations are closed, they can be solved numerically by open source software SU2[26]. Finite volume method is applied to discretize governing equation. To capture the shock, which is discontinuous on flow variables, a high Total Variation Diminishing(TVD) method is resorted to. In this work, 2nd order Roe method is applied. Since we mainly focus on steady flow, the term

related to time in governing equations can be neglected. Meanwhile, an implicit pseudo-time stepping approach is adopted to replace the time term. The initial Courant-Friedrichs-Lewy(CFL) number is 1. The values of CFL number up and down factor are 1.1 and 0.1, respectively. FGMRES method is chosen for linear solver. The convergence criteria is that either the simulation runs up to maximum 100000 steps or the residual of conservative variables is lower than -12. In case viscous calculation are carried out, one equation Spalart-Allmaras (SA) turbulence model is chosen due to its simplicity and popularity in aerospace field. Besides, axisymmetric option is turned on.

2.2.4 Geometry and boundary conditions

The computational domain of the current numerical simulation is a rectangular box field outside the nozzle, illustrated in figure 2.2. The nozzle itself is not simulated but the reference geometry is taken from paper[4]. As we can see, the axial and radial axes are normalized by the diameter of nozzle exit D and the geometry of nozzle is shown in figure 2.3. Hence, the non-dimension size of this box is 10×2.5, which is large enough to obtain the accurate solution referring to previous work[3]. The domain is divided by unstructured triangular grid, refined near the nozzle inlet and the symmetry axis. This kind of mesh is generated by Gmsh and the mesh near the inlet is shown in figure 2.4. Along the axis direction, the minimum dimensionless mesh size, which is normalized by nozzle exit diameter D, of the triangle element is $h = 0.02$ so that the position of Mach disk can be located up to two decimal places. What's more, along the radial direction, the radius of Mach disk can be positioned up to three decimal places.

Four types of boundary conditions are applied:

1. The inlet($x = 0; 0 \leq y \leq 0.5$) boundary condition is a supersonic inlet, where the inlet pressure, temperature, velocity are prescribed;
2. The wall($x = 0; 0.5 \leq y \leq 2.5$) is a non-slip wall;
3. The centerline($y = 0$) is symmetric;
4. Non-reflecting Riemann boundary condition is imposed on top($y = 2.5$) and outlet($x = 10$), where only static pressure is needed.

Once the flow variables at the nozzle exit(also the inlet of the current computational domain) are known[3], the variables at the nozzle reservoir can be computed from equation 2.1.

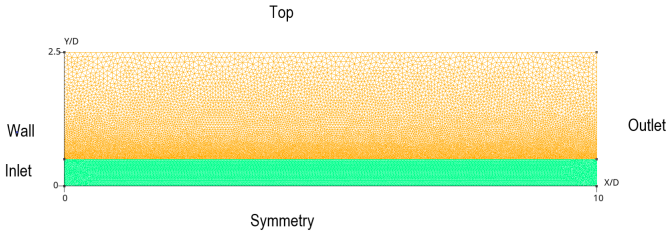

Figure 2.2: Computational domain

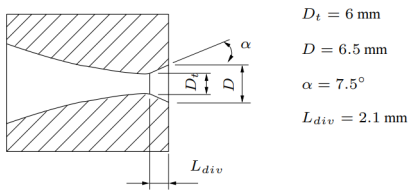

Figure 2.3: Nozzle geometry 1.5C from [4]

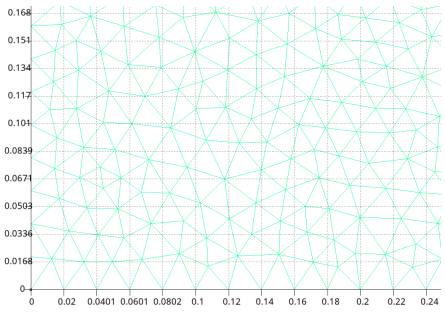

Figure 2.4: Zoom of mesh near the inlet

Chapter 3

Numerical results

In this chapter, the main results of numerical simulations are reported and compared with previous studies. Results of underexpanded jets with reservoir-to-ambient pressure ratio 8 are demonstrated firstly, then results with pressure ratio 10 are discussed.

3.1 Underexpanded jet with pressure ratio 8

In this section, four types of simulations are investigated: ideal inviscid, non-ideal inviscid, ideal viscous and non-ideal viscous flows.

3.1.1 Ideal inviscid flow

The main aim of this section is to validate the numerical simulation of this work by comparing with previous results. The test case IG-8 from [3] is chosen and the related flow variables are shown in table 3.1. The gas is nitrogen and reservoir-to-ambient pressure ratio $\beta = P_0/P_a$ is 8, which results in the nozzle exit-to-ambient pressure ratio is 2.97 for the nozzle in figure 2.3. Based on the geometry and boundary conditions with $h = 0.02$ presented in section 2.2, the simulation converges and the residual history is shown in figure 3.1. As can be seen, residuals of all conservative variables decreases with iteration. The blue line, representing the residual of density, is lower than -12 after around 1200 step of iterations, which satisfies the convergence criteria.

Grid convergence

Grid convergence solution is obtained by making mesh more fine.The pressure distribution along the centerline is given in figure 3.2, with respect to different mesh size h. The mesh related to blue line

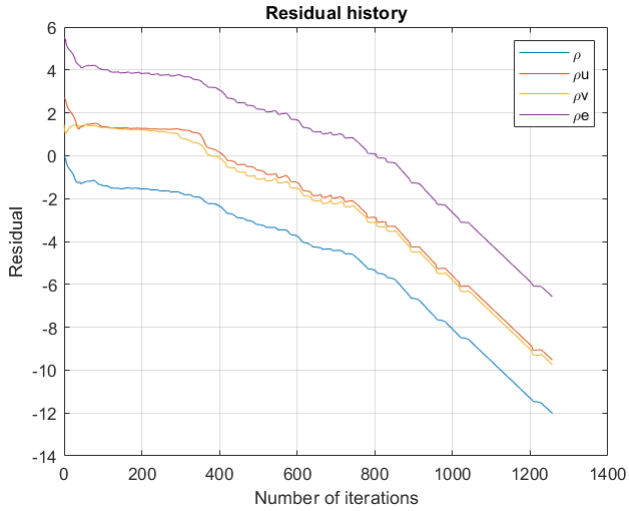

Figure 3.1: Residual history with $h = 0.02$

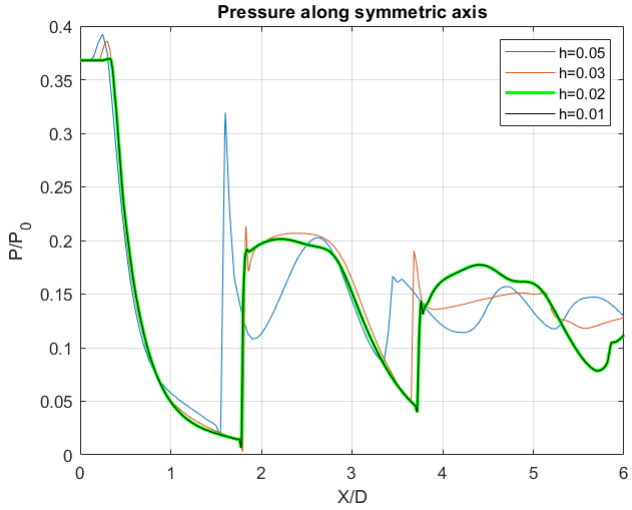

Figure 3.2: Pressure along the axis with different mesh size

$h = 0.05$ is relatively coarse and its pressure near the Mach disk oscillates violently. By comparison, the red line stands for the mesh $h = 0.03$ and its pressure near the Mach disk oscillates smoothly. In addition, its Mach disk moves downstream along the centerline. The solution corresponding to fine mesh $h = 0.02$, is the green curve. Obviously, its pressure near the Mach disk changes very smooth without oscillation. If we decrease the mesh size further to $h = 0.01$, it is found that the pressure distribution overlaps with that of $h = 0.02$. Therefore, we can conclude that the mesh with

$h = 0.02$ are capable of resulting in grid convergence solution. For the fine mesh, the computational domains are divided into 20151 points and 57568 unstructured triangle elements. This fine mesh is applied for all simulations in this thesis. Summary of results with different mesh size are listed in table 3.2.

Name	Symbol	Value
Nitrogen	N_2	–
Critical pressure	P_c	$3.39 \times 10^6\ Pa$
Critical temperature	T_c	$126.15\ K$
Critical volume	v_c	$3.18 \times 10^{-3}\ m^3/kg$
Critical density	ρ_c	$3.14 \times 10^2\ kg/m^3$
Reservoir pressure	P_0	$8.03 \times 10^5\ Pa$
Reservoir volume	v_0	$1.25 \times 10^{-1}\ m^3/kg$
Reservoir density	ρ_0	$8.01\ kg/m^3$
Reservoir Temperature	T_0	$3.37 \times 10^2\ K$
Ambient pressure	P_a	$1.00 \times 10^5\ Pa$
Ambient temperature	T_a	$2.70 \times 10^2\ K$
Ambient density	ρ_a	$1.25\ kg/m^3$
Exit pressure	P_e	$2.98 \times 10^5\ Pa$
Exit temperature	T_e	$2.52 \times 10^2\ K$
Exit mach number	M_e	1.287
Specific ratio	γ	1.4
Specific gas constant	R	$297\ J/Kg \cdot K$
Compressibility factor at nozzle exit	Z_e	1

Table 3.1: IG-8 case properties

Mesh size h	Number of points	Number of elements	Position of Mach disk
0.01	85554	172112	1.79
0.02	20151	57568	1.79
0.03	15123	30584	1.78
0.05	6840	13884	1.52

Table 3.2: Summary of different mesh size results

Flow field analysis

The final solution of Mach field is depicted in figure 3.3. It is clear that the flow is supersonic before the Mach disk and becomes subsonic across it. To show the flow features clearly, the contour of density is plotted in figure 3.4. Firstly, Prandtl-Mayer expansion waves move from the nozzle exit and compression waves combine into interception shock, which reflects on the Mach disk and forms reflected shock. A slip line, which delimits the outer supersonic flow and inner subsonic flow, extends from the triple point.

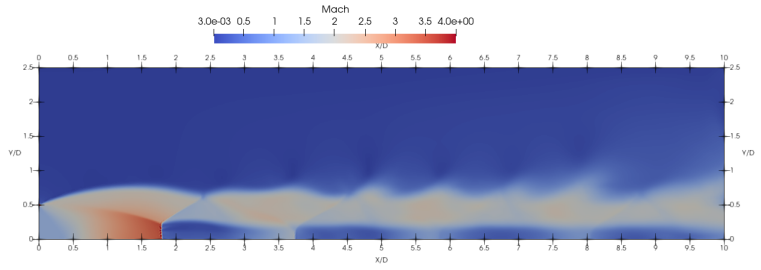

Figure 3.3: Flow field of Mach number in IG-8 case

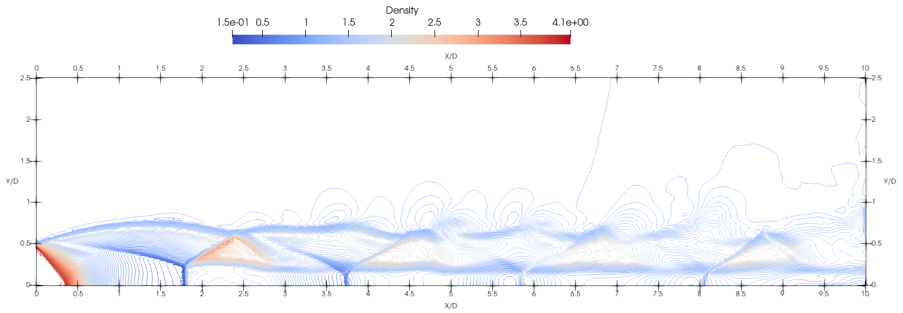

Figure 3.4: Contour of density in IG-8 case

Now we compare our result with previous data from [3]. Firstly, the position and radius of Mach disk are compared and their values are listed in table 3.3, where $x_m/D, r_m/D$ are the position and radius of Mach disk, normalized by nozzle exit diameter D. In the current simulation, the position of Mach disk is more far from the nozzle exit and its radius is a little larger. The Mach number, pressure

Data type	x_m/D	r_m/D	β	Z_e
Ideal invicid case	1.79	0.230	8	1
A.G. 2007[3]	1.72	0.220	8	1

Table 3.3: Position and radius of Mach disk from A.G 2007 and ideal invicid case $P_0/P_a = 8$

normalized by reservoir pressure P_0 along the symmetry axis are plotted in figure 3.5. In total, the numerical results of Mach and pressure distribution along centerline agree with those from [3] well, especially around the Mach disk. After $X/D = 4$, these results differ because that the mesh in that region is relatively coarse. Overall, the simulation results from this work match with previous results well and hence the current results are validated, considering that nozzle is neglected in this work.

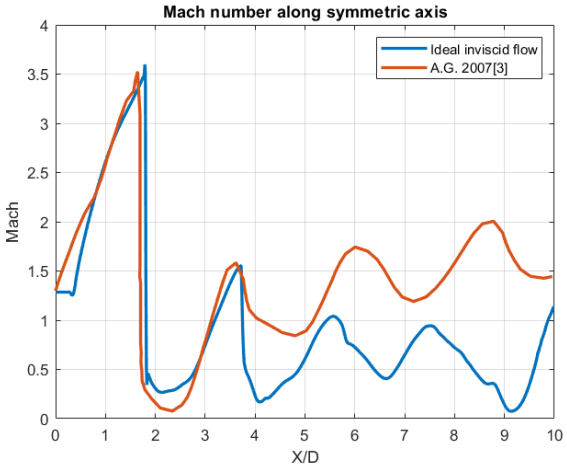

(a) Mach number along symmetry axis

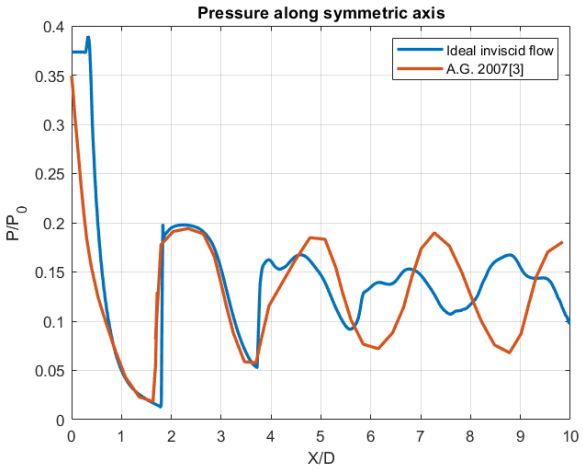

(b) Pressure along symmetry axis

Figure 3.5: Comparison of Mach, pressure along symmetry axis for ideal inviscid flow $P_0/P_a = 8$

Effect of pressure level

Now, the exit-to-ambient pressure ratio P_e/P_a is kept constant while their absolute values increase α times, in order to check whether the pressure level influences the flow field. The values of flow variables are listed in table 3.4, where $I-I$ means *ideal inviscid*. Meanwhile, all other flow variables, like temperature, Mach number at the exit are unchanged. The Mach number and pressure along the centerline are illustrated in figure 3.6.

Case name	P_e	P_a	P_e/P_a	α	β	Z_e
I-I-8-1	$2.98 \times 10^5\ Pa$	$1.00 \times 10^5\ Pa$	2.97	1	8	1
I-I-8-3	$8.94 \times 10^5\ Pa$	$3.01 \times 10^5\ Pa$	2.97	3	8	1
I-I-8-5	$1.49 \times 10^6\ Pa$	$5.02 \times 10^5\ Pa$	2.97	5	8	1

Table 3.4: Pressure in different cases for ideal inviscid gas $P_0/P_a = 8$

The Mach number and pressure distributions are almost same. Hence, like the isentropic flow in a nozzle, the flow field of under-expanded jets outside the nozzle for PIG also only depends on the exit-to-ambient pressure ratio, regardless of the exit condition.

Conclusion

In this subsection, grid convergence solution is obtained firstly; then the flow field of simulation is analyzed; the results of this work match well with previous work[3][4]; finally, it is found that the flow field of ideal inviscid case is independent on pressure level.

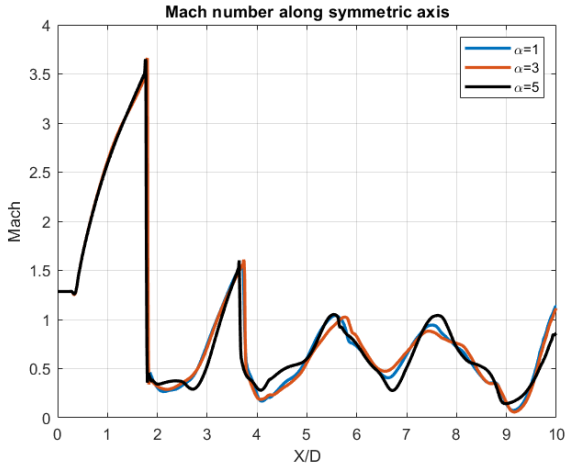

(a) Mach number along symmetry axis of different pressure level $P_0/P_a = 8$

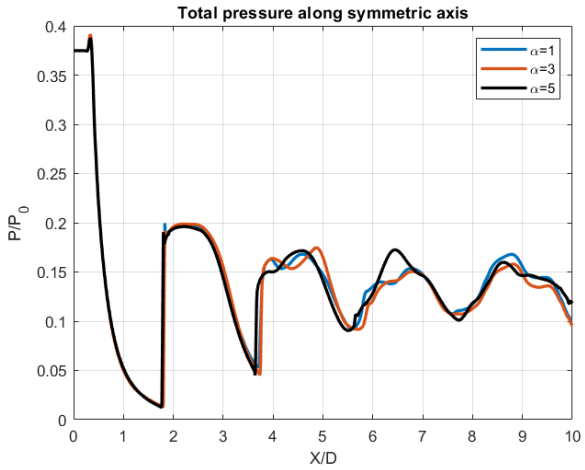

(b) Pressure along symmetry axis of different pressure level $P_0/P_a = 8$

Figure 3.6: Mach, pressure along symmetry axis of different pressure level $P_0/P_a = 8$

3.1.2 Non-ideal inviscid flow

First of all, the non-ideal inviscid flow is simulated and polytropic van der Waals(VW) model is activated. The values of flow variables imposed as boundary conditions are same with IG-8 case and all data are listed in table 3.1.

Flow field analysis

The flow field of Mach number is compared with that of ideal inviscid case, shown in figure 3.7. The main flow features, including

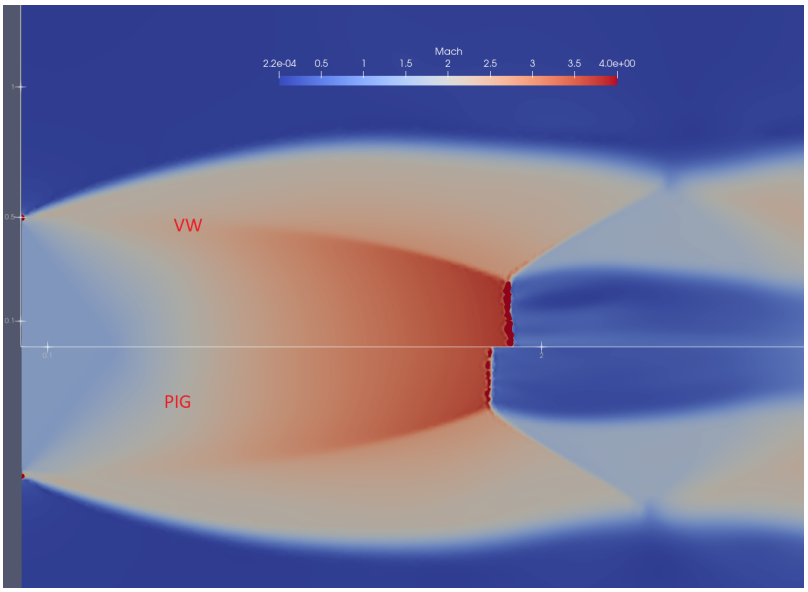

Figure 3.7: Mach field of VW and PIG gas for inviscid flow, $P_0/P_a = 8$

interception shock, reflected shock, slip line and Mach disk, are captured in both cases, except that the position and radius of Mach disk are slightly different. The Mach number and pressure along the symmetry axis are plotted in figure 3.8. The main difference is that the position of Mach disk of VW model is more far from the nozzle exit compared with PIG. The results of Mach disk in both cases are listed in table 3.5. Alongside, to illustrate the non-ideality, compressibility factor Z is compared, shown in figure 3.9. For PIG, Z is constant and equal to unit. By contrast, Z of VW model oscillates between 0.95 and 1, which verifies the non-ideality of VW gas.

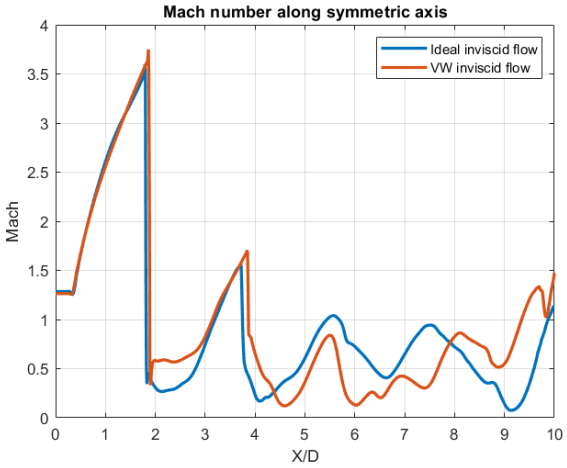

(a) Mach number along symmetry axis for ideal and VW inviscid flow $P_0/P_a = 8$

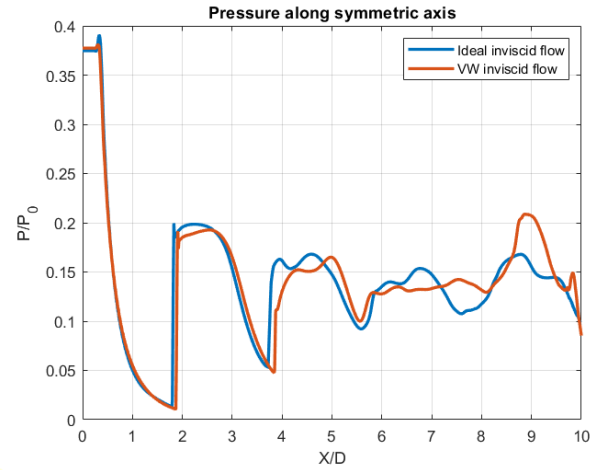

(b) Pressure along symmetry axis for ideal and VW inviscid flow $P_0/P_a = 8$

Figure 3.8: Mach, pressure along symmetry axis for ideal and VW inviscid flow $P_0/P_a = 8$

Data type	x_m/D	r_m/D	β	Z_e
Ideal inviscid case	1.79	0.230	8	1
VW inviscid case	1.86	0.240	8	0.950

Table 3.5: Position and radius of Mach disk for ideal and VW inviscid case $P_0/P_a = 8$

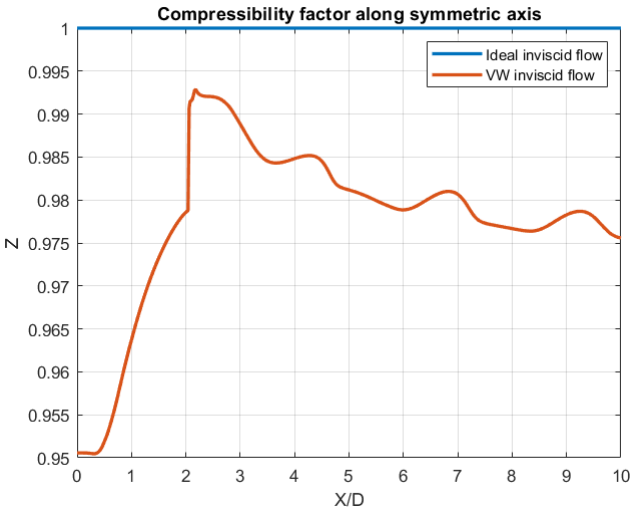

Figure 3.9: Compressibility factor along symmetry axis for ideal and VW inviscid flow $P_0/P_a = 8$

Effect of pressure level

Now, the pressure values are same with PIG case in table 3.4 again. The results of Mach disk are summarized in table 3.6, where $V - I$ means *VW inviscid*: With higher P_e, the distance of Mach disk to

Case name	x_m/D	r_m/D	α	β	Z_e
V-I-8-1	1.86	0.240	1	8	0.950
V-I-8-3	1.93	0.231	3	8	0.948
V-I-8-5	2.01	0.190	5	8	1.015

Table 3.6: Summary of Mach disk in VW invicid case $P_0/P_a = 8$

nozzle exit is larger while its radius is smaller. Mach number and pressure with $\alpha = 1, 3, 5$ along the symmetry axis are plotted in figure 3.10. It can be found that with higher P_e, the Mach number and pressure after the Mach disk are larger.

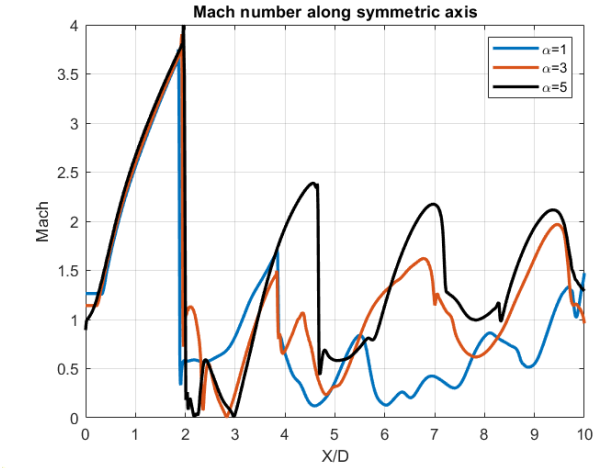

(a) Mach number along symmetry axis of VW inviscid flow $P_0/P_a = 8$

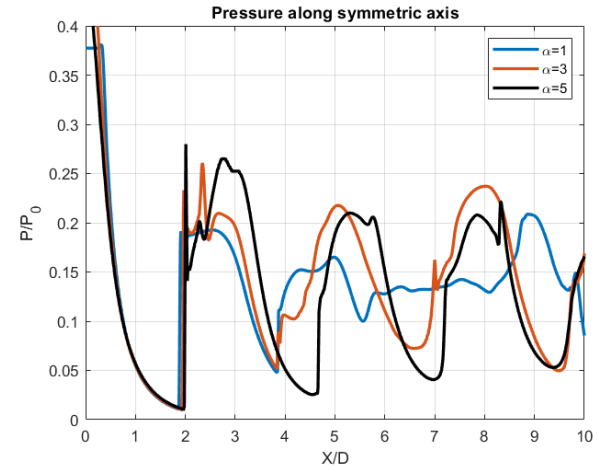

(b) Pressure along symmetry axis of VW inviscid flow $P_0/P_a = 8$

Figure 3.10: Mach, pressure along symmetry axis for VW inviscid flow with different exit condition $P_0/P_a = 8$

Conclusion

In this subsection, simulation result of non-ideal VW model inviscid case is compared with ideal inviscid case under same conditions; in VW case, position of Mach disk is more downstream and its radius is a little larger; then effect of pressure level is investigated. With higher pressure level, position of Mach disk is more downstream and the radius decreases.

3.1.3 Ideal viscous gas

Ideal viscous flow is simulated with same values of flow variables imposed as boundary conditions in table 3.1 except the viscosity is considered. The Sutherland model is applied to compute the viscosity. RANS governing equations and SA turbulence model are activated.

Flow field analysis

The Mach field of ideal inviscid and viscous flow are shown in figure 3.11. Compared with ideal inviscid flow, th distance of Mach disk

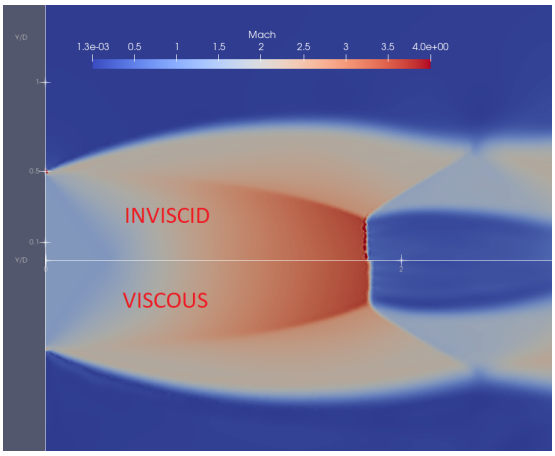

Figure 3.11: Mach field of ideal inviscid and viscous flow with $P_0/P_a = 8$

to nozzle exit in ideal viscous flow is a little larger and its radius also increases. Results of Mach disk are listed in table 3.7: The

Data type	x_m/D	r_m/D	β	Z_e
Ideal inviscid case	1.79	0.230	8	1
Ideal viscous case	1.80	0.250	8	1

Table 3.7: Position and radius of Mach disk for ideal inviscid and viscous case $P_0/P_a = 8$

comparison of Mach number and pressure along symmetry axis is shown in figure 3.12: Compared with ideal inviscid case, the position of Mach disk move downstream along axial direction in ideal viscous case. In other words, for PIG, the effect of viscosity is to delay the formation of Mach disk, although the effect is very small.

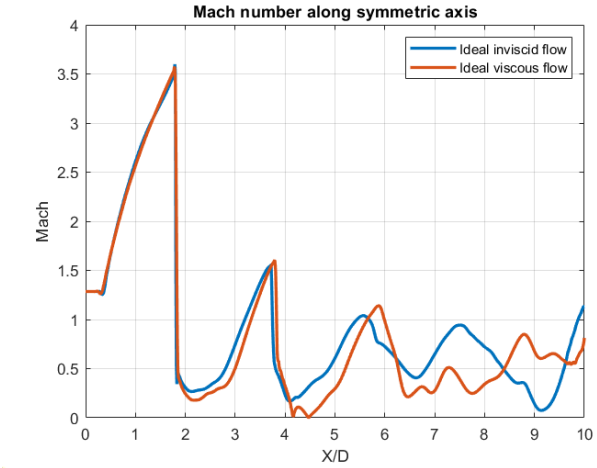

(a) Mach number along symmetry axis for ideal inviscid and viscous flow $P_0/P_a = 8$

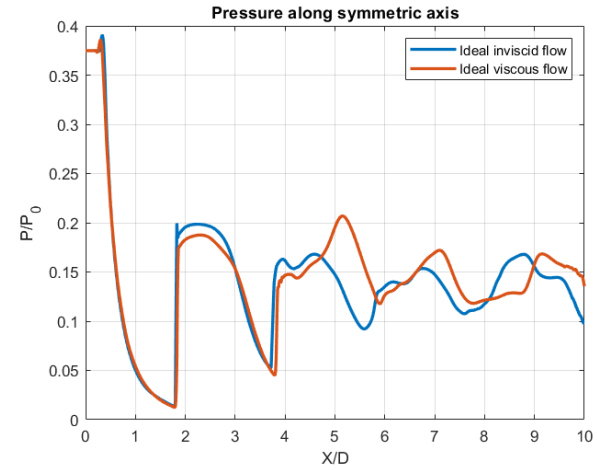

(b) Pressure along symmetry axis for ideal inviscid and viscous flow $P_0/P_a = 8$

Figure 3.12: Mach, pressure along symmetry axis for ideal inviscid and viscous flow $P_0/P_a = 8$

Effect of pressure level

Again, the effect of pressure level is carried out. The Mach number and pressure with different α are plotted in figure 3.13. Mach number and pressure are same before $X/D = 4$ and differ with each other after $X/D = 4$ due to coarse mesh.

Conclusion

In this subsection, simulation result of ideal viscous flow is compared with ideal inviscid flow; the effect of viscosity is to delay the formation of Mach disk. Besides, the flow field is independent on reservoir condition.

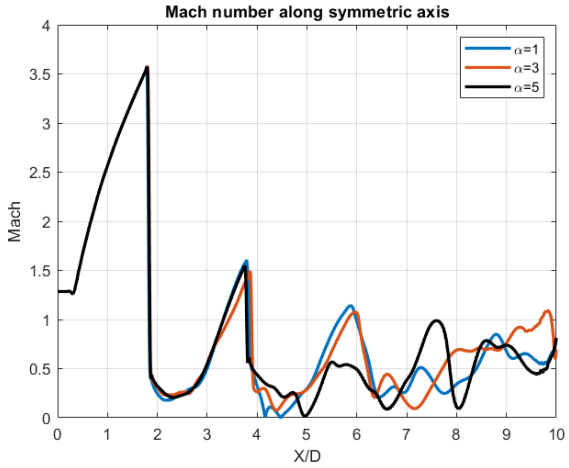

(a) Mach number along symmetry axis of ideal viscous flow $P_0/P_a = 8$

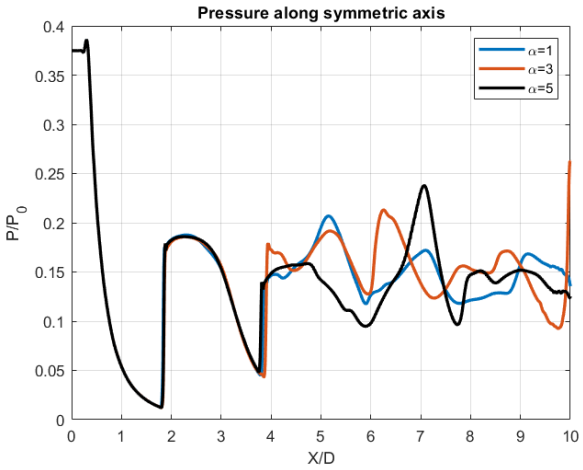

(b) Pressure along symmetry axis of ideal viscous flow $P_0/P_a = 8$

Figure 3.13: Mach, pressure along symmetry axis for ideal viscous flow with different exit condition $P_0/P_a = 8$

3.1.4 Non-ideal viscous flow

VW viscous flow is simulated with same values of flow variables imposed as boundary conditions in table 3.1.

Flow field analysis

The Mach field is compared for VW inviscid and viscous flow, shown in figure 3.14. As shown in previous section, the viscosity for PIG

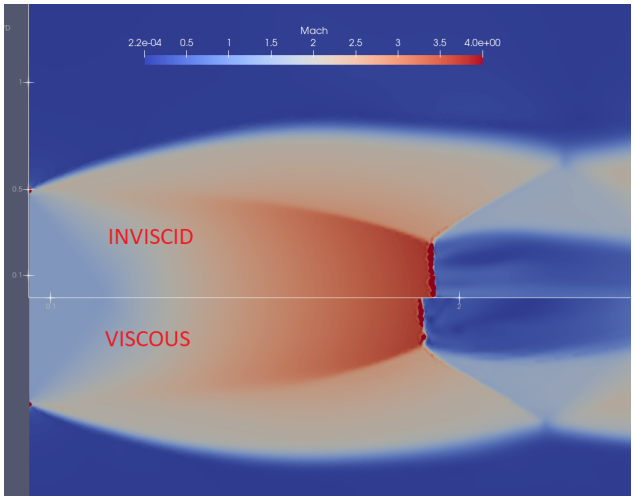

Figure 3.14: Mach field of VW inviscid and viscous flow with $P_0/P_a = 8$

makes the Mach disk more far from the nozzle exit and increases its radius. However, this effect is exactly adverse for non-ideal VW gas. Namely, the position of Mach disk is closer to nozzle exit and its radius is smaller in VW viscous flow, compared with VW inviscid flow. Also, this effect of viscosity is stronger in VW case than that in PIG case. The results of Mach disk are listed in table 3.8. The

Data type	x_m/D	r_m/D	β	Z_e
VW inviscid case	1.86	0.240	8	0.950
VW viscous case	1.82	0.231	8	0.996

Table 3.8: Position and radius of Mach disk for VW inviscid and viscous case $P_0/P_a = 8$

related Mach number and pressure along symmetry axis are plotted in figure 3.15.

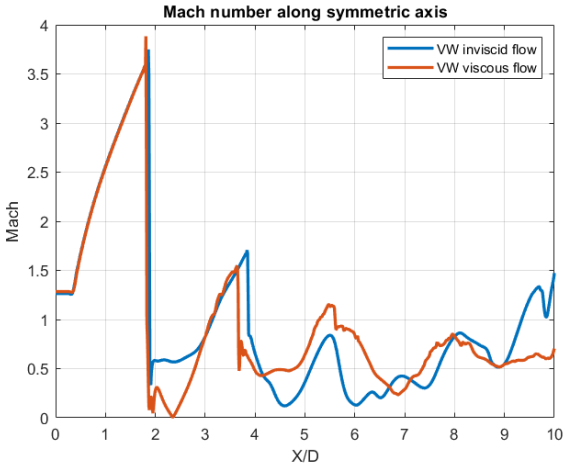

(a) Mach number along symmetry axis for VW inviscid and viscous flow $P_0/P_a = 8$

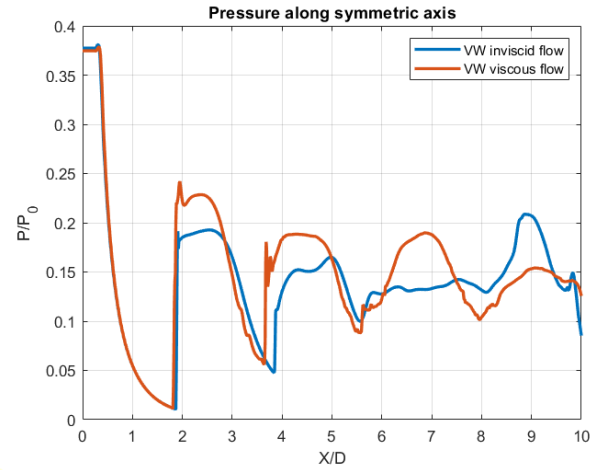

(b) Pressure along symmetry axis for VW inviscid and viscous flow $P_0/P_a = 8$

Figure 3.15: Mach, pressure along symmetry axis for VW inviscid and viscous flow $P_0/P_a = 8$

Effect of pressure level

Again, the pressure values are same with PIG case in table 3.4. The results of Mach disk are summarized in table 3.9: With higher P_e, the Mach disk moves downstream along axial direction while its radius increases. The Mach number and pressure along symmetry

Case name	x_m/D	r_m/D	α	β	Z_e
V-V-8-1	1.82	0.231	1	8	0.950
V-V-8-3	1.84	0.247	3	8	0.948
V-V-8-5	1.86	0.254	5	8	1.015

Table 3.9: Summary of Mach disk in VW viscous case $P_0/P_a = 8$

axis of different α are shown in figure 3.16.

Conclusion

In this subsection, simulation result of VW viscous flow is compared with VW inviscid case; Mach disk moves upstream and its radius decreases in the viscous case. With higher pressure level, Mach disk moves downstream and its radius increases.

3.1.5 Summary

In this section, Data of Mach disk in all cases are summarized in table 3.10, where I-I,V-I,I-V,V-V represent ideal inviscid, VW inviscid, ideal viscous, VW viscous cases. To show the combined effect of vis-

Case name	x_m/D	r_m/D	α	β	Z_e
I-I-8-1	1.79	0.230	1	8	1
I-I-8-3	1.79	0.230	3	8	1
I-I-8-5	1.79	0.230	5	8	1
V-I-8-1	1.86	0.240	1	8	0.950
V-I-8-3	1.93	0.231	3	8	0.948
V-I-8-5	2.01	0.190	5	8	1.015
I-V-8-1	1.80	0.250	1	8	1
I-V-8-3	1.80	0.250	3	8	1
I-V-8-5	1.80	0.250	5	8	1
V-V-8-1	1.82	0.231	1	8	0.950
V-V-8-3	1.84	0.247	3	8	0.948
V-V-8-5	1.86	0.254	5	8	1.015

Table 3.10: Summary of Mach disk in all cases of $P_0/P_a = 8$

cosity and non-ideality, Mach number and pressure along symmetry axis of ideal inviscid and VW viscous cases with $\alpha = 1$ are plotted in

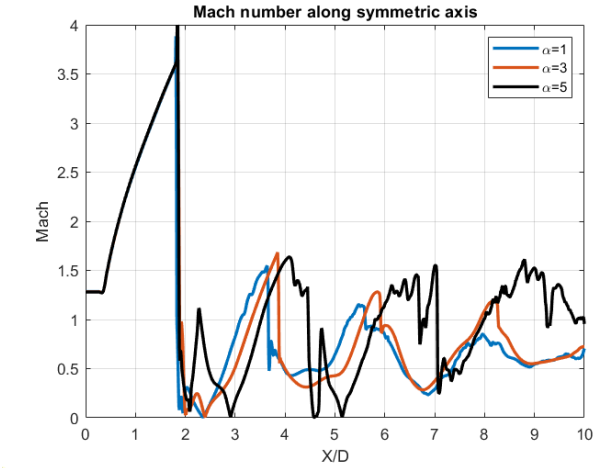

(a) Mach number along symmetry axis of VW viscous flow $P_0/P_a = 8$

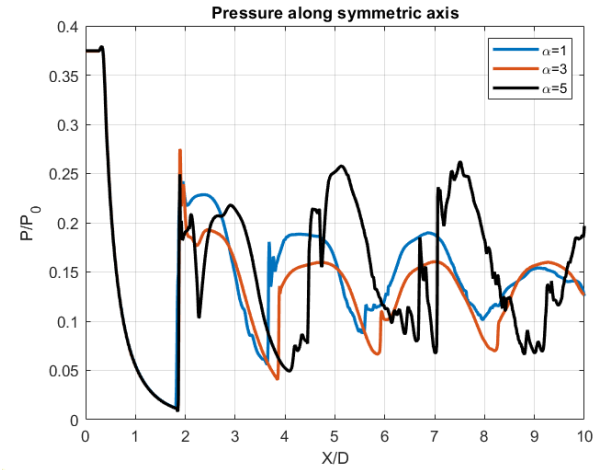

(b) Pressure along symmetry axis of VW viscous flow $P_0/P_a = 8$

Figure 3.16: Mach, pressure along symmetry axis for VW viscous flow with different exit condition $P_0/P_a = 8$

figure 3.17. From table 3.10, the Mach disk is more downstream and has larger radius in VW viscous case, compared with ideal inviscid counterpart.

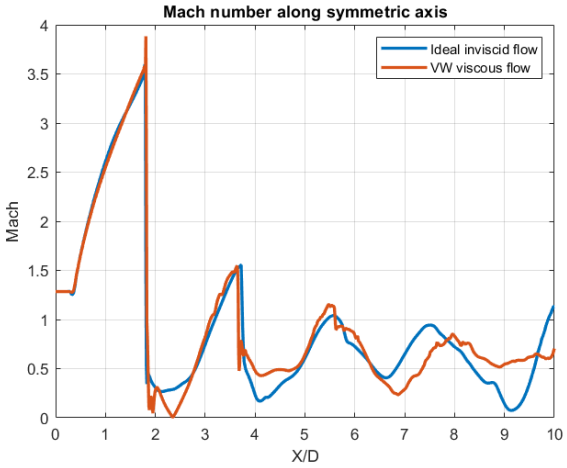

(a) Mach number along symmetry of ideal inviscid and VW viscous flow with $P_0/P_a = 8$

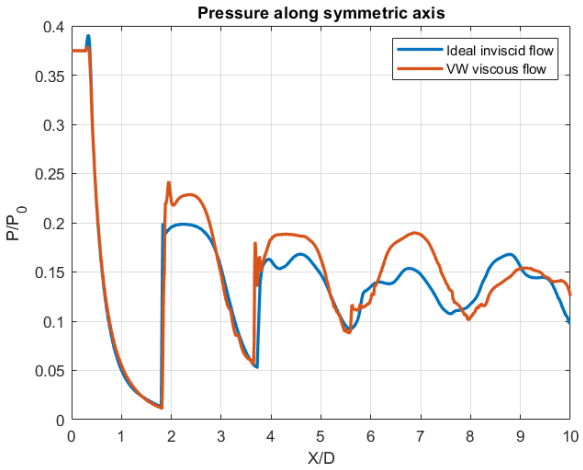

(b) Pressure along symmetry axis of ideal inviscid and VW viscous flow with $P_0/P_a = 8$

Figure 3.17: Mach number and pressure along symmetry axis of ideal inviscid and VW viscous flow with $P_0/P_a = 8$

3.2 Underexpanded jets with pressure ratio 10

3.2.1 Ideal inviscid flow

Flow field analysis

The ideal inviscid flow with $P_0/P_a = 10$ is simulated. In this case, $P_e/P_a = 3.72$. The related flow variables can be found in IG-10 case[3]. The results of Mach disk are compared with previous work[3], listed in table 3.11. In this work, the position of Mach disk is more downstream and its radius is a little larger. Both errors of position and radius are 5%, which are reasonably considering that nozzle is not simulated. The Mach number and pressure along

Data type	x_m/D	r_m/D	β	Z_e
Ideal invicid case	1.79	0.230	8	1
Ideal invicid case	2.08	0.340	10	1
A.G. 2007[3]	1.98	0.324	10	1

Table 3.11: Results of position and radius of Mach disk $P_0/P_a = 10$

symmetry axis are shown in figure 3.18.

Effect of pressure ratio

Here, the Mach fields of ideal inviscid flow with $\beta = P_0/P_a = 8, 10$ are compared, to explore the effect of pressure ratio. As can be seen from figure 3.19, with higher pressure ratio $P_0/P_a = 10$, the Mach disk moves downstream and has larger radius; the comparison of Mach disk can be found in table 3.11. The Mach number, pressure along symmetry axis are plotted in figure 3.20. The difference between Mach disk is obvious; for $\beta = 10$ case, the change of Mach number across Mach disk is more rapid, which indicates its Mach disk is stronger.

Effect of pressure level

Again, the flow variables are same with IG-10 case[3] but different pressure level are applied. The case names and pressure level are listed in table 3.12. The Mach field of $\alpha = 1, 5$ are compared, shown

Case name	P_e	P_a	P_e/P_a	α	β	Z_e
I-I-10-1	$3.76 \times 10^5\ Pa$	$1.01 \times 10^5\ Pa$	3.72	1	10	1
I-I-10-3	$1.13 \times 10^6\ Pa$	$3.03 \times 10^5\ Pa$	3.72	3	10	1
I-I-10-5	$1.88 \times 10^6\ Pa$	$5.05 \times 10^5\ Pa$	3.72	5	10	1

Table 3.12: Pressure in different cases for ideal inviscid gas $P_0/P_a = 10$

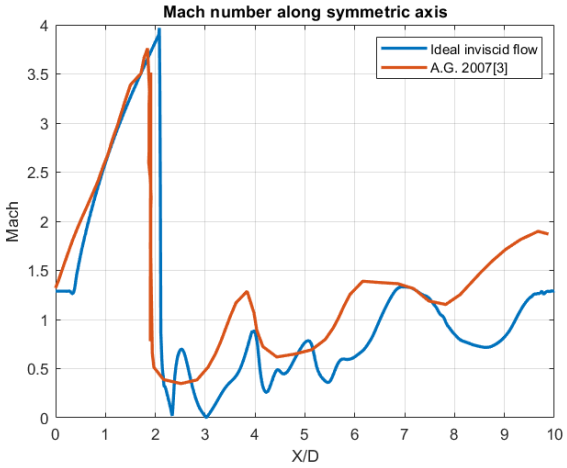

(a) Mach number along symmetry axis for ideal inviscid flow $P_0/P_a = 10$

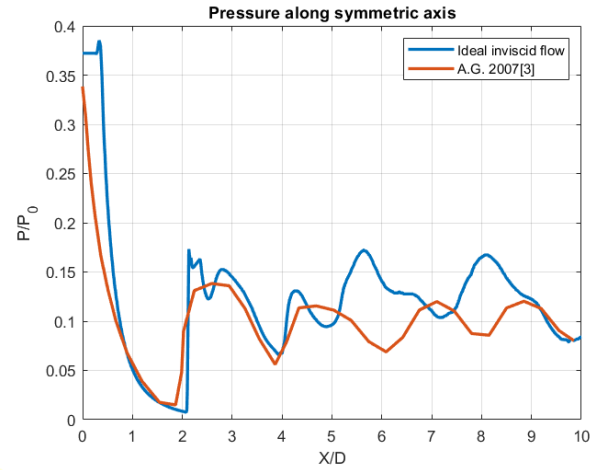

(b) Pressure along symmetry axis for ideal inviscid flow $P_0/P_a = 10$

Figure 3.18: Mach, pressure along symmetry axis for ideal inviscid flow $P_0/P_a = 10$

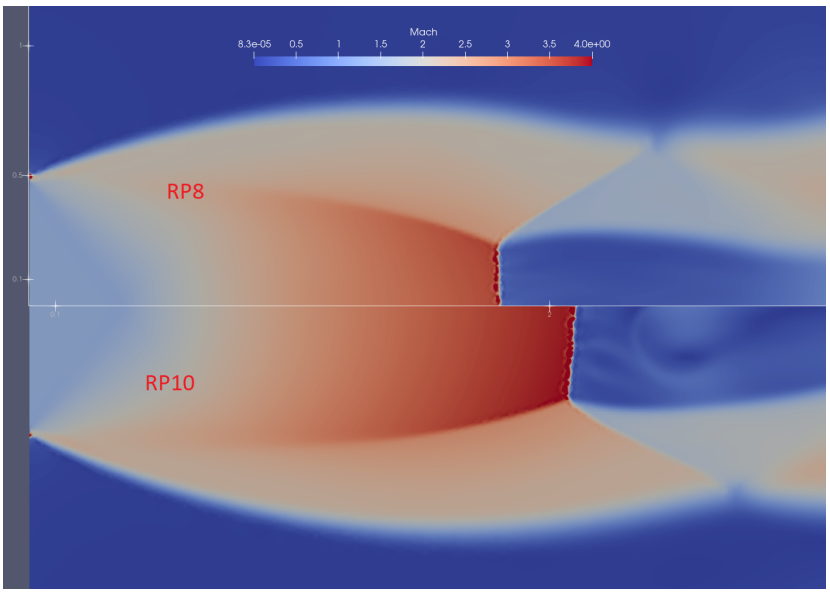

Figure 3.19: Mach field of ideal inviscid flow with $P_0/P_a = 8, 10$

in figure 3.21. The Mach field are same until around $X/D = 4$, after that the mesh is coarse. Hence, it can be concluded that the ideal inviscid flow with $\beta = 10$ is also independent on pressure level. For brevity, the Mach number and pressure along symmetry axis are not plotted here.

Conclusion

In this subsection, simulation results of ideal inviscid flow with $\beta = 10$ are validated by comparing with previous work[3]; in addition, the ideal inviscid flow is independent on pressure level.

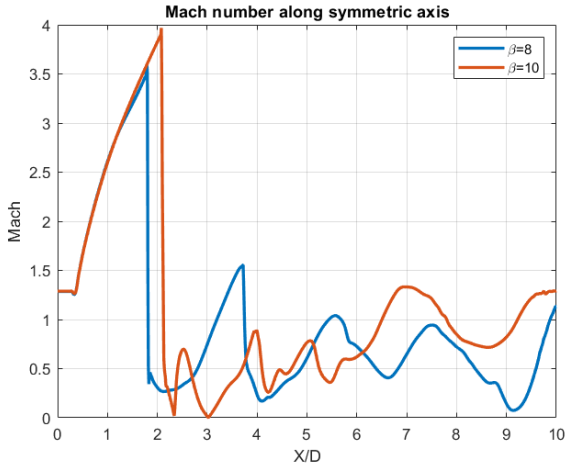

(a) Mach number along symmetry axis for ideal inviscid flow $P_0/P_a = 8, 10$

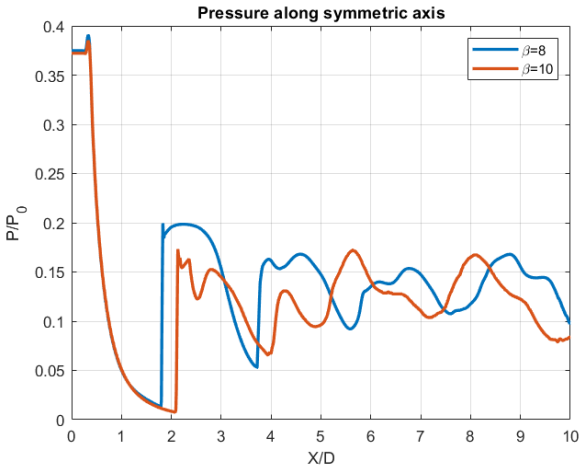

(b) Pressure along symmetry axis for ideal inviscid flow $P_0/P_a = 8, 10$

Figure 3.20: Mach, pressure along symmetry axis for ideal inviscid flow $P_0/P_a = 8, 10$

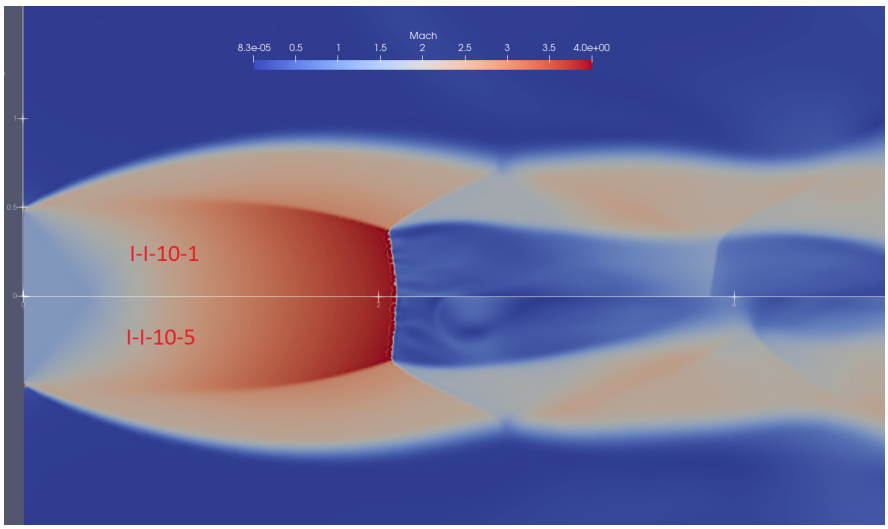

Figure 3.21: Mach field of ideal inviscid flow with $\alpha = 1, 5, P_0/P_a = 10$

3.2.2 Non-ideal inviscid flow

In this subsection, non-ideal VW model is activated. Same values of flow variables imposed as boundary conditions in IG-10 case[3].

Flow field analysis

The Mach field of ideal and VW inviscid flow are compared, shown in figure 3.22. The Mach disk in VW case is more downstream and has smaller radius. The result of Mach disk in listed in table 3.13. Related Mach number and pressure along symmetry axis are plotted in figure 3.23.

Effect of pressure level

The effect of pressure level is investigated and results of Mach disk are summarized in table 3.13. With higher pressure level, the Mach disk moves downstream and has smaller radius. Related Mach number and pressure along symmetry axis are plotted in figure 3.24.

Case name	x_m/D	r_m/D	α	β	Z_e
I-I-10-1	2.08	0.340	1	10	1
V-I-10-1	2.16	0.330	1	10	0.998
V-I-10-3	2.18	0.320	3	10	0.994
V-I-10-5	2.20	0.313	5	10	0.991

Table 3.13: Summary of Mach disk in VW invicid case $P_0/P_a = 10$

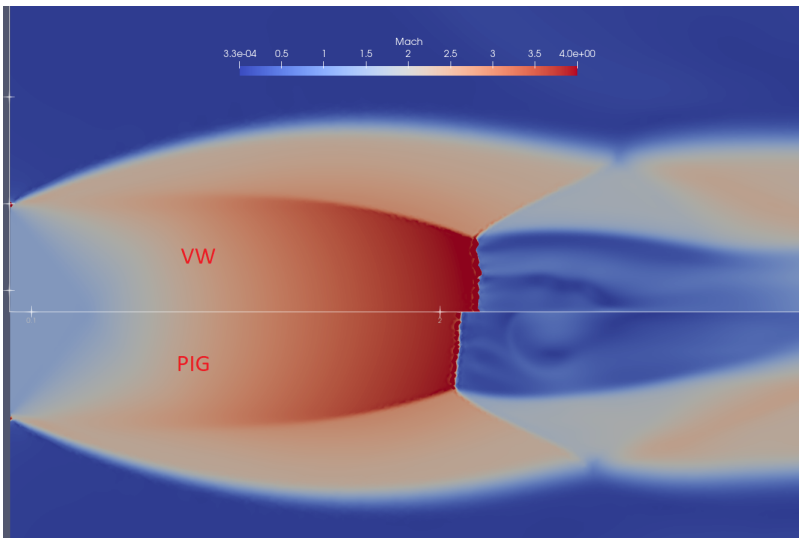

Figure 3.22: Mach field of ideal and VW inviscid flow with $P_0/P_a = 10$

Conclusion

In this subsection, simulation results of VW inviscid flow are compared with ideal inviscid case; Mach disk moves downstream and has smaller radius in VW case. Besides, with higher pressure level, the distance of Mach disk to nozzle exit is larger and its radius decreases.

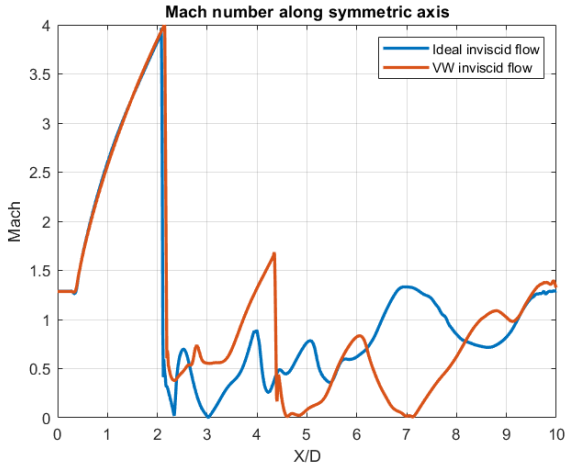

(a) Mach number along symmetry axis for ideal and VW inviscid flow $P_0/P_a = 10$

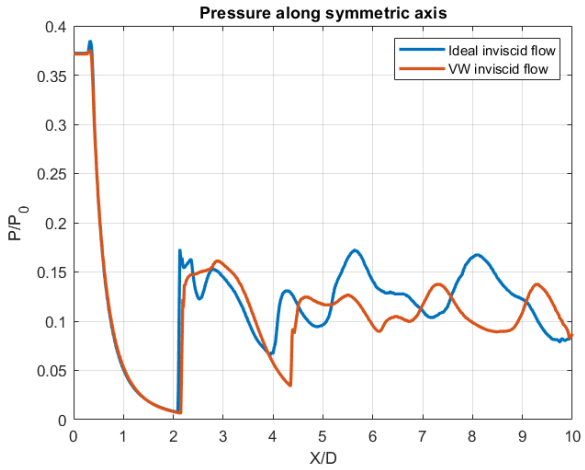

(b) Pressure along symmetry axis for ideal and VW inviscid flow $P_0/P_a = 10$

Figure 3.23: Mach, pressure along symmetry axis for ideal and VW inviscid flow $P_0/P_a = 10$

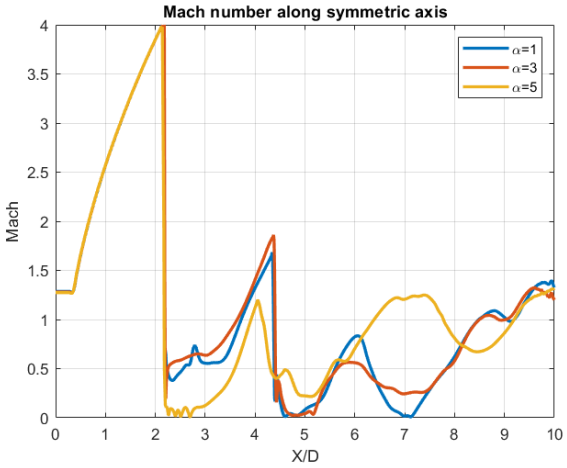

(a) Mach number along symmetry axis of VW inviscid flow $P_0/P_a = 10$

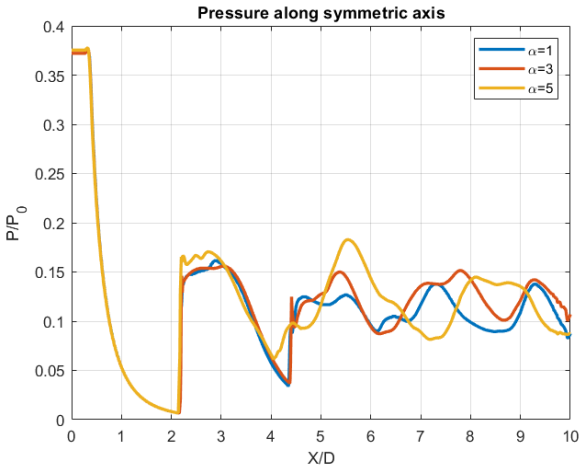

(b) Pressure along symmetry axis of VW inviscid flow $P_0/P_a = 10$

Figure 3.24: Mach, pressure along symmetry axis for VW inviscid flow with different exit condition $P_0/P_a = 10$

3.2.3 Ideal viscous flow

In this subsection, Sutherland viscosity model is applied and Spalart-Allmaras (SA) turbulence model is activated. Same values of flow variables imposed as boundary conditions in IG-10 case[3].

Flow field analysis

The Mach field of ideal inviscid and viscous flow are compared in figure 3.25. The Mach disk is more downstream and has larger radius. The results of Mach disk are listed in table 3.14. Again, the effect of viscosity in PIG case is small. The related Mach number and pressure along symmetry axis are plotted in figure 3.26.

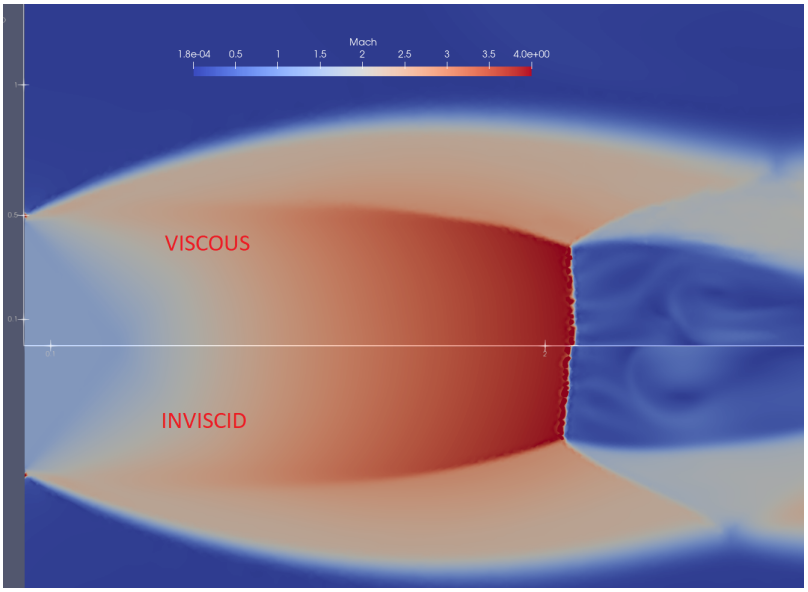

Figure 3.25: Mach field of ideal inviscid and viscous flow with $P_0/P_a = 10$

Data type	x_m/D	r_m/D	β	Z_e
Ideal inviscid case	2.08	0.340	10	1
Ideal viscous case	2.09	0.345	10	1

Table 3.14: Results of position and radius of Mach disk $P_0/P_a = 10$

Effect of pressure level

Same flow variables with IG-10 case[3] but higher pressure level are applied, listed in table 3.15. The Mach field of $\alpha = 1, 5$ are compared in figure 3.27. The Mach field are same before $X/D = 4$. Hence, the ideal viscous flow is independent on pressure level.

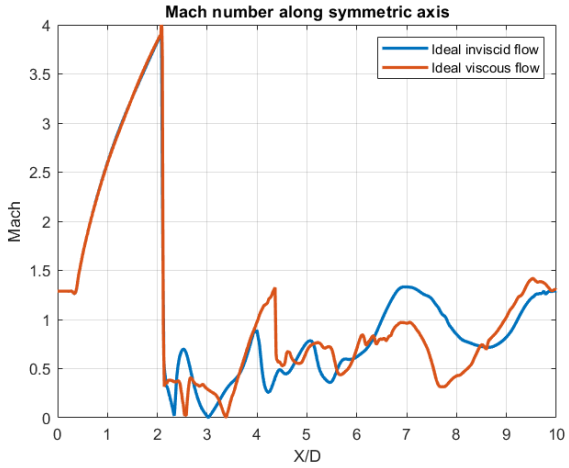

(a) Mach number along symmetry axis for ideal inviscid and viscous flow $P_0/P_a = 10$

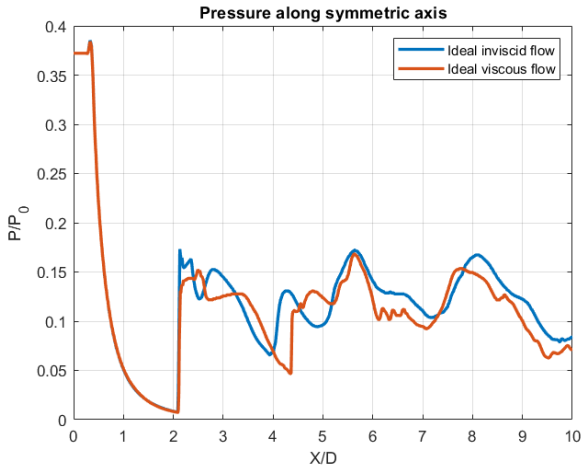

(b) Pressure along symmetry axis for ideal inviscid and viscous flow $P_0/P_a = 10$

Figure 3.26: Mach, pressure along symmetry axis for ideal inviscid and viscous flow $P_0/P_a = 10$

Case name	P_e	P_a	P_e/P_a	α	β	Z_e
I-V-10-1	$3.76 \times 10^5\ Pa$	$1.01 \times 10^5\ Pa$	3.72	1	10	1
I-V-10-3	$1.13 \times 10^6\ Pa$	$3.03 \times 10^5\ Pa$	3.72	3	10	1
I-V-10-5	$1.88 \times 10^6\ Pa$	$5.05 \times 10^5\ Pa$	3.72	5	10	1

Table 3.15: Pressure in different cases for ideal viscous gas $P_0/P_a = 10$

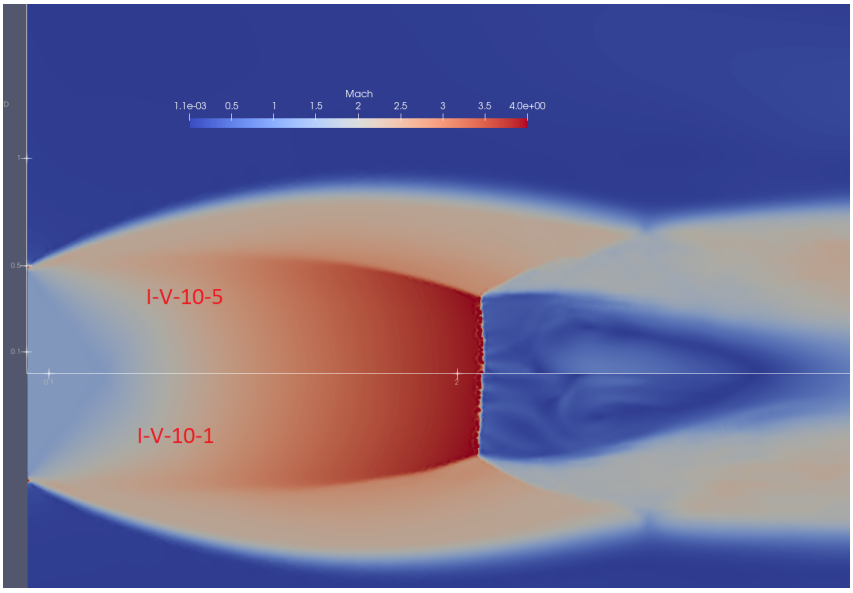

Figure 3.27: Mach field of ideal viscous flow with $\alpha = 1, 5; P_0/P_a = 10$

Conclusion

In this subsection, simulation result of ideal viscous flow is compared with ideal inviscid case; the Mach disk is a little more downstream and has larger radius in viscous case. The pressure level does not affect the flow field.

3.2.4 Non-ideal viscous flow

Same values of flow variables imposed as boundary conditions in IG-10 case[3].

Flow field analysis

The Mach field of VW viscous flow is compared with VW inviscid case, shown in figure 3.28. The result of Mach disk can be found in table 3.16. The Mach disk in viscous case is more upstream and has larger radius. Again, the effect os viscosity in VW case is stronger than that in PIG case. The related Mach number and pressure along symmetry axis are plotted in figure 3.29.

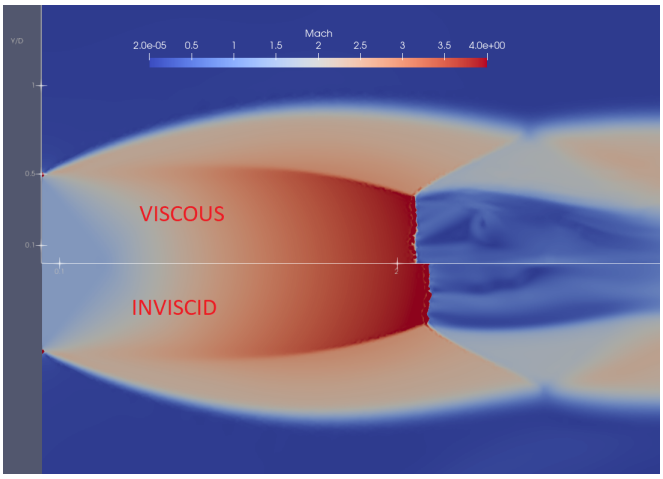

Figure 3.28: Mach field of VW inviscid and viscous flow with $P_0/P_a = 10$

Effect of pressure level

The effect of pressure level is carried out again. The results of Mach disk are listed in table 3.16. The related Mach number and pressure along symmetry axis are plotted in figure 3.30. With higher pressure level, Mach disk moves downstream and has smaller radius.

Case name	x_m/D	r_m/D	α	β	Z_e
V-I-10-1	2.16	0.330	1	10	0.998
V-V-10-1	2.12	0.366	1	10	0.998
V-V-10-3	2.15	0.361	3	10	0.994
V-V-10-5	2.19	0.345	5	10	0.991

Table 3.16: Summary of Mach disk in VW viscous case $P_0/P_a = 10$

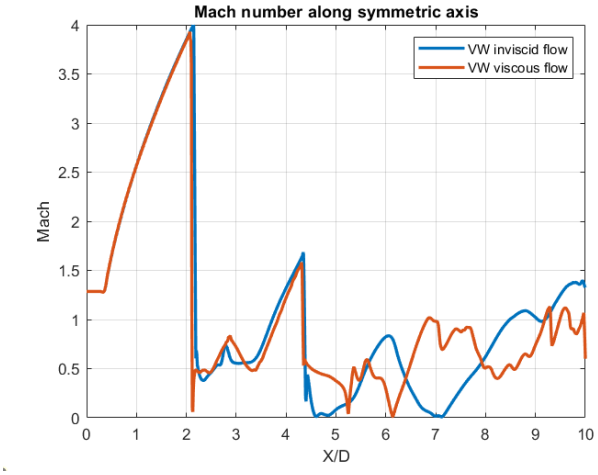

(a) Mach number along symmetry axis for VW inviscid and viscous flow $P_0/P_a = 10$

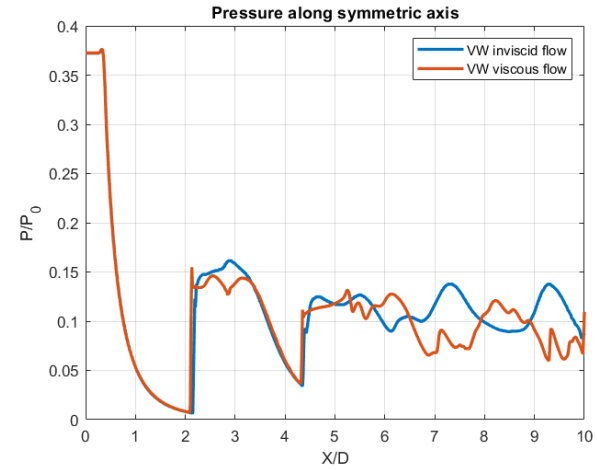

(b) Pressure along symmetry axis for VW inviscid and viscous flow $P_0/P_a = 10$

Figure 3.29: Mach, pressure along symmetry axis for VW inviscid and viscous flow $P_0/P_a = 10$

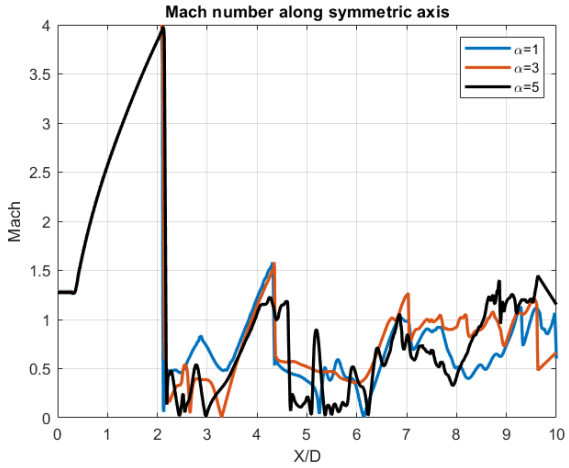

(a) Mach number along symmetry axis of VW viscous flow $P_0/P_a = 10$

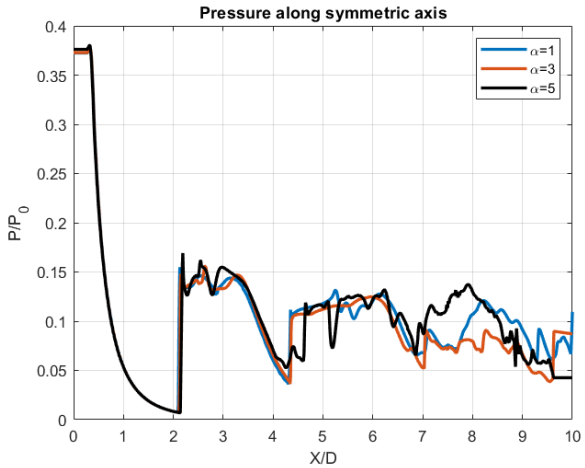

(b) Pressure along symmetry axis of VW viscous flow $P_0/P_a = 10$

Figure 3.30: Mach, pressure along symmetry axis for VW viscous flow with different exit condition $P_0/P_a = 10$

Conclusion

In this subsection, simulation result of VW viscous flow is compared with VW inviscid case; the Mach disk is a little more upstream and has larger radius. With higher pressure level, Mach disk moves downstream and has smaller radius.

3.2.5 Summary

In this section, Data of Mach disk in all cases are summarized in table 3.17, where I-I,V-I,I-V,V-V represent ideal inviscid, VW inviscid, ideal viscous, VW viscous cases. To show the combined effect of viscosity and non-ideality, Mach number and pressure along symmetry axis of ideal inviscid and VW viscous cases with $\alpha = 1$ are plotted in figure 3.31. From table 3.17, the Mach disk is more downstream and has larger radius in VW viscous case, compared with ideal inviscid counterpart.

Case name	x_m/D	r_m/D	α	β	Z_e
I-I-10-1	2.08	0.340	1	10	1
I-I-10-3	2.08	0.340	3	10	1
I-I-10-5	2.08	0.340	5	10	1
V-I-10-1	2.16	0.330	1	10	0.998
V-I-10-3	2.18	0.320	3	10	0.994
V-I-10-5	2.20	0.313	5	10	0.991
I-V-10-1	2.09	0.345	1	10	1
I-V-10-3	2.09	0.345	3	10	1
I-V-10-5	2.09	0.345	5	10	1
V-V-10-1	2.12	0.366	1	10	0.998
V-V-10-3	2.15	0.361	3	10	0.994
V-V-10-5	2.19	0.345	5	10	0.991

Table 3.17: Summary of Mach disk in all cases of $P_0/P_a = 10$

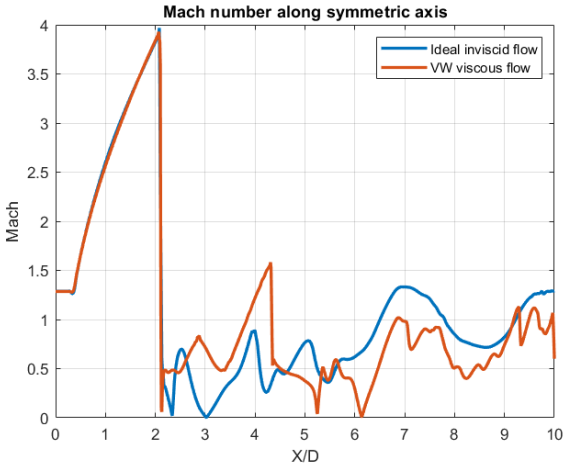

(a) Mach number along symmetry of ideal inviscid and VW viscous flow with $P_0/P_a = 10$

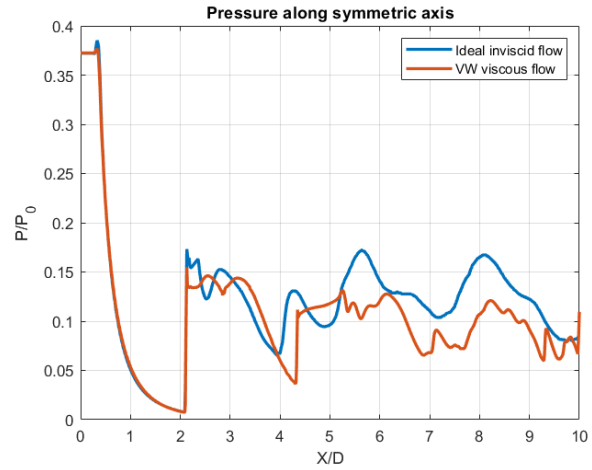

(b) Pressure along symmetry axis of ideal inviscid and VW viscous flow with $P_0/P_a = 10$

Figure 3.31: Mach number and pressure along symmetry axis of ideal inviscid and VW viscous flow with $P_0/P_a = 10$

Chapter 4

Conclusion

4.1 Conclusion

In this work, underexpanded jet flow is simulated with open-source code SU2. The simulations are divided into two categories with pressure ratio $\beta = 8, 10$; each category contain four types of cases: ideal inviscid, VW inviscid, ideal viscous and VW viscous flow. In each type of case, three kinds of flow with different pressure level are carried. Totally, 24 kinds of cases are simulated. The main conclusion are as following:

1. **Validation.**
   The results of ideal inviscid flow with $\beta = 8, 10$ are compared with previous work[3]; the errors of position and radius of Mach disk are within 5%, which is a reasonable agreement considering that the nozzle itself is not simulated.

2. **Effect of non-ideality.** Compared with ideal flow, the Mach disk moves downstream in both cases $\beta = 8, 10$; with $\beta = 8$, VW flow has larger radius in inviscid case while smaller radius in viscous case; with $\beta = 10$, VW flow has smaller radius in inviscid case while larger radius in viscous case;

3. **Effect of pressure ratio.**
   In same condition of ideal inviscid flow, the Mach disk with higher pressure ratio $\beta = 10$ is more downstream and has larger radius, compared with the case of $\beta = 8$.

4. **Effect of pressure level.**
   In both categories $\beta = 8, 10$, the ideal flow is independent on pressure level α; for VW model with higher α, the Mack disk moves downstream in both cases while its radius increases in $\beta = 8$ and decreases in $\beta = 10$.

5. **Effect of viscosity.**
   In both categories $\beta = 8, 10$, the Mach disk moves downstream and has larger radius in ideal viscous case, compared with ideal inviscid counterpart; in VW viscous case, Mach disk moves upstream. However, Mach disk has smaller radius with $\beta = 8$ and larger one with $\beta = 10$, compared with VW inviscid case. Besides, the effect of viscosity is stronger in VW case than that in PIG case in both categories.

6. **Combined effect of viscosity and non-ideality.**
   In both categories $\beta = 8, 10$ with same pressure level α, the Mach disk is more downstream and has larger radius in VW viscous case, compared with its ideal inviscid counterpart.

4.2 Further plan

Although the main focus in this work is the position and radius of Mach disk, some problems still need to be investigated further:

1. The total pressure after Mach disk increases rapidly in the experiment[4] while it varies smoothly in the inviscid simulation. The author[4] thought the viscosity could help recover the behavior of total pressure in the experiment. Recovery of total pressure are to be done in the further investigation.

2. More accurate non-ideal gas models need to be carried out, including Peng-Robinson gas model.

3. Gas dynamics non-ideal cases with $\Gamma < 1$ need to be researched.

Bibliography

[1] DAVIDE Vimercati. *Non-Ideal Steady Supersonic Flows*. PhD thesis, Ph. D. thesis, Politecnico di Milano, 2019.

[2] Philip A Thompson. A fundamental derivative in gasdynamics. *The Physics of Fluids*, 14(9):1843–1849, 1971.

[3] A Guardone, M Parsani, and Luigi Vigevano. Numerical simulations of under-expanded nozzle flows of dense gases. In *XVIII Congress of the Italian Association of Theoretical and Applied Mechanics (AIMETA)*, pages 1–9, 2007.

[4] H Katanoda, Y Miyazato, M Masuda, and K Matsuo. Pitot pressures of correctly-expanded and underexpanded free jets from axisymmetric supersonic nozzles. *Shock waves*, 10(2):95–101, 2000.

[5] Johannes Diderik Van der Waals. *Over de Continuiteit van den Gas-en Vloeistoftoestand*, volume 1. Sijthoff, 1873.

[6] D Berthelot. Travaux et memoires du bureau international des poids et mesures tome xiii. *Gauthier-Villars, Paris*, 1907.

[7] Ding-Yu Peng and Donald B Robinson. A new two-constant equation of state. *Industrial & Engineering Chemistry Fundamentals*, 15(1):59–64, 1976.

[8] Davide Vimercati, Giulio Gori, and Alberto Guardone. Non-ideal oblique shock waves. *Journal of Fluid Mechanics*, 847:266–285, 2018.

[9] Alberto Matteo Attilio Guardone. Nozzle design for supersonic flows of n2o at supercritical and close-to-critical conditions. In *8th International Conference on Flow Dynamics*, pages 1–2, 2011.

[10] Jacques Fages, Hubert Lochard, Jean-Jacques Letourneau, Martial Sauceau, and Elisabeth Rodier. Particle generation

for pharmaceutical applications using supercritical fluid technology. *Powder Technology*, 141(3):219–226, 2004.

[11] Gerd Brunner. Supercritical fluids: technology and application to food processing. *Journal of food engineering*, 67(1-2):21–33, 2005.

[12] Andrea Spinelli, Giorgia Cammi, Camilla Cecilia Conti, Simone Gallarini, Marta Zocca, Fabio Cozzi, Paolo Gaetani, Vincenzo Dossena, and Alberto Guardone. Experimental observation and thermodynamic modeling of non-ideal expanding flows of siloxane mdm vapor for orc applications. *Energy*, 168:285–294, 2019.

[13] A Kluwick. Non-ideal compressible fluid dynamics: a challenge for theory. In *Journal of Physics: Conference Series*, volume 821, page 012001. IOP Publishing, 2017.

[14] T Mathijssen, M Gallo, E Casati, NR Nannan, C Zamfirescu, A Guardone, and P Colonna. The flexible asymmetric shock tube (fast): a ludwieg tube facility for wave propagation measurements in high-temperature vapours of organic fluids. *Experiments in Fluids*, 56(10):1–12, 2015.

[15] Alberto Guardone, Andrea Spinelli, and Vincenzo Dossena. Influence of molecular complexity on nozzle design for an organic vapor wind tunnel. *Journal of engineering for gas turbines and power*, 135(4), 2013.

[16] Adam Joseph Head, Carlo De Servi, Emiliano Casati, Matteo Pini, and Piero Colonna. Preliminary design of the orchid: a facility for studying non-ideal compressible fluid dynamics and testing orc expanders. In *Turbo Expo: Power for Land, Sea, and Air*, volume 49743, page V003T25A001. American Society of Mechanical Engineers, 2016.

[17] Barbara Re, Cécile Dobrzynski, and Alberto Guardone. Assessment of grid adaptation criteria for steady, two-dimensional, inviscid flows in non-ideal compressible fluids. *Applied Mathematics and Computation*, 319:337–354, 2018.

[18] Bin Zang, Vevek US, and Tze How D New. Openfoam based numerical simulation study of an underexpanded supersonic jet. In *55th AIAA Aerospace Sciences Meeting*, page 0747, 2017.

[19] Salvatore Vitale, Giulio Gori, Matteo Pini, Alberto Guardone, Thomas D Economon, Francisco Palacios, Juan J Alonso, and Piero Colonna. Extension of the su2 open source cfd code to

the simulation of turbulent flows of fuids modelled with complex thermophysical laws. In *22nd AIAA Computational Fluid Dynamics Conference*, page 2760, 2015.

[20] Gianfranco Angelino and Piero Colonna Di Paliano. Multicomponent working fluids for organic rankine cycles (orcs). *Energy*, 23(6):449–463, 1998.

[21] Shigeru Obayashi. Numerical simulation of underexpanded plumes using upwind algorithms. In *15th Atmospheric Flight Mechanics Conference*, page 4360, 1988.

[22] Francesco Bonelli, Annarita Viggiano, and Vinicio Magi. A numerical analysis of hydrogen underexpanded jets under real gas assumption. *Journal of Fluids Engineering*, 135(12), 2013.

[23] Grazia Lamanna, Ernst Oldenhof, Steffen Baab, Ingo Stotz, and Bernhard Weigand. Disintegration regimes near the critical point. In *18th AIAA/3AF International Space Planes and Hypersonic Systems and Technologies Conference*, page 5914, 2012.

[24] Luigi Crocco. Considerations on the shock-boundary layer interaction. In *Proc. Conf. on High-Speed Aeron*, pages 75–112, 1955.

[25] Michael Abbett. Mach disk in underexpanded exhaust plumes. *AIAA Journal*, 9(3):512–514, 1971.

[26] Thomas D Economon, Francisco Palacios, Sean R Copeland, Trent W Lukaczyk, and Juan J Alonso. Su2: An open-source suite for multiphysics simulation and design. *Aiaa Journal*, 54(3):828–846, 2016.

Appendix A

Nomenclature

Γ Fundamental derivative of gas dynamics
γ ratio of specific heats
s specific entropy
P pressure
T temperature
ρ density
v specific volume
P_0 reservoir pressure
P_e pressure at the nozzle exit
P_a ambient pressure
P^t total pressure
T^t total temperature
T_e temperature at the nozzle exit
ρ^t total density
M Mach number
t time
$\mathbf{m}$ vector of axial and radial momentum $(m_x.m_y)$
E^t total energy per unit volume
$\mathbf{u}$ vector of $(\rho, \mathbf{m}, E^t)$
$\mathbf{f}(u)$ flux function of $\mathbf{u}$
Ω computational domain
C control volume
∂C boundary of control volume
$\mathbf{n}$ outward unit vector normal to ∂C
$\mathbf{I}$ identity matrix
$\mathcal{R}$ universal gas constant
R specific gas constant
$\mathcal{M}$ molecular weight
a parameter related to van der Waals model
b parameter related to van der Waals model

c_v specific heat at constant volume
P_c critical pressure
T_c critical temperature
v_c critical specific volume
h mesh size
x_m normalized position of Mach disk
r_m normalized radius of Mach disk
Z comprehensibility factor
Z_e comprehensibility factor at nozzle exit

Appendix B

Acronym

PIG polytropic ideal gas
NICFD non-ideal compressible fluid dynamics
CFD computational fluid dynamics
ORC Organic Rankine Cycle
TVD Total Variation Diminishing
CFL Courant-Friedrichs-Lewy
EOS equations of state
RANS Reynolds-averaged Navier?Stokes
VW van der Waals
SA Spalart-Allmaras